International Journal of Earth Sciences
https://doi.org/10.1007/s00531-021-02118-5

ORIGINAL PAPER

Tectonics and fluvial dynamism affecting the Tiber River in Prehistoric Rome

F. Marra[1] · A. L. Brock[2] · F. Florindo[1,6] · P. Macrì[1] · L. Motta[3] · C. Nicosia[4] · N. Terrenato[5]

Received: 7 June 2021 / Accepted: 21 September 2021

Abstract

Geomorphological investigations in Rome's river valley are revealing the dynamism of the prehistoric landscape. It is becoming increasingly apparent that paleogeographic conditions that defined Rome in the historical era are the product of changes since the Bronze Age, which may be the result of local fault activity in addition to fluvial dynamism. Through a dedicated borehole chronostratigraphic study, integrated by ^{14}C and archaeological dates, and paleomagnetic investigations, we offer here new evidence for fault displacement since ca. 4500 years/BP. We present the failure of the sedimentary fabric of a clay horizon caused by liquefaction processes commonly linked with seismic shaking, interpreting an (ca. 4 m) offset to signify the existence of a fault line located at the foot of the Capitoline Hill. In addition, we show evidence for another (ca. 1 m) offset affecting a stratigraphic horizon in the river channel, occurring along another hypothesized fault line crossing through the Tiber Valley. Movement along this fault may have contributed to a documented phase of fast overflooding dated to the sixth century BCE which eventually led to the birth of the Tiber Island. The most plausible scenario implies progressive deformation, with an average tectonic rate of 2 mm/year, along these inferred fault lines. This process was likely punctuated with moderate earthquakes, but no large event necessarily occurred. Together, the available evidence suggests that during the early centuries of sedentary habitation at the site of Rome, active fault lines contributed to significant changes to the Tiber River valley, capable of challenging lowland activities.

Keywords Pre-urban Rome · Tiber Island · Coring survey · Alluvial stratigraphy · Paleomorphology · Faulting · Fluvial dynamics

Introduction

Recent geomorphological investigations performed across the area of the ancient city known as the Forum Boarium have revealed a dramatic paleogeographic transformation in Rome's central river valley that occurred sometime between the Bronze Age (ca. 4500 years/BP) and the Archaic Period (6th c. BCE; 2550-2450/BP) (Marra et al. 2018; Brock et al. 2021).

Based on combined geomorphological analysis and borehole data, these authors suggest that this process of hydrological change and landscape transformation was the result, at least in part, of progressive movement along an NW–SE striking fault zone aligned with the Murcia Valley and crossing through the Tiber Valley. Besides providing new accommodation space for sediment accumulation, such faulting activity could have been responsible for diversions of the river course and the creation of the Tiber Island within a fault-controlled river bend.

✉ F. Marra
fabrizio.marra@ingv.it

1 Istituto Nazionale di Geofisica e Vulcanologia, Via di Vigna Murata 605, 00143 Rome, Italy

2 School of Classics, University of St Andrews, Swallowgate, St Andrews KY16 9AL, UK

3 Kelsey Museum of Archaeology, University of Michigan, 434 S. State St, Ann Arbor, MI 48109-1390, USA

4 Dipartimento Dei Beni Culturali, Università Di Padova, Padova, Italy

5 Department of Classical Studies, University of Michigan, 435 S. State St, Ann Arbor, MI 48109-1003, USA

6 Institute for Climate Change Solutions, Via Sorchio, 61040 Frontone, Italy

Published online: 08 October 2021

In this study, we present the results of a new drilling campaign, which was aimed at recovering idiosyncratic chronostratigraphic markers and providing further evidence on the occurrence, displacement, and the timing of the hypothesized faulting process that arguably affected the alluvial sediments of the Tiber River.

Morpho-stratigraphic setting of the Tiber Valley

The investigated area is characterized by a complex geomorphological setting (e.g., Del Monte et al. 2016), originated by the convergence of two tributary valleys of the Tiber River, the Murcia and the Velabrum (Fig. 1). During the last glacial lowstand, the streams flowing in these valleys eroded the pyroclastic surface formed by the products of the Monti Sabatini and Colli Albani Volcanic Districts, separating the Capitoline, Palatine, and Aventine hills with deep incisions. These appeared as isolated plateaus emerging from the flat-bottomed alluvial plains after the completion of the post-glacial sea-level rise, around 6000 year BP. However, millennia of anthropic activity have smoothed the terrain by filling the alluvial plains and modifying the slopes of the hillsides (Luberti et al. 2018).

The valley of the Tiber River (Fig. 1) was deeply incised as a consequence of the pronounced sea-level fall during the Last Glacial Maximum (Marra et al. 2013, 2016a; Marra and Florindo 2014). The base of the sedimentary fill deposited in response to sea-level rise since ca. 18,000 years/BP during the Last Glacial Termination (LGT) is 37 m below sea level in the Forum Boarium area (Marra et al. 2018) and reaches ~ 45 m b.s.l. in correspondence of the central axis of the Tiber Valley (Corazza et al. 1999; Marra et al. 2013). A coarse gravel layer up to 8 m thick rests above the basal erosive surface in the deepest portion of the incision, while it lacks or it is replaced by a colluvial fan at higher elevation along the valley flanks. Paleoclimatic data and geochronologic ages constrain the deposition of this gravel in the interval 18,000–12,800 years/BP (Marra et al. 2013, 2016a). An abrupt upward transition to a several m-thick package of sandy clay sediments occurs throughout the Tiber channel. The sedimentary switch is bracketed in the interval 15,000–12,800 years/BP, coinciding with the meltwater pulse MPW-1 during the LGT (Stanford et al. 2011; Marra et al. 2016a). By 6000 years/BP an organic-rich, clayey aggradational deposit filled the fluvial incisions reaching up to the present sea-level elevation. At this age an estuarine environment was established through the present coastal area as well as in the river valley through the city of Rome, and it is characterized by a temporarily emerging alluvial plain at 1–2 m a.s.l. (Marra et al. 2018).

Re-incision of this early alluvial plain around 5500 years/BP down to 10 m b.s.l. is documented by the unconformable contact with the overlaying, fining-upward succession of yellow sandy-clay sediments and by the occurrence of a cm-sized gravel layer, a few decimeters thick, in the deepest portion of the new river channel

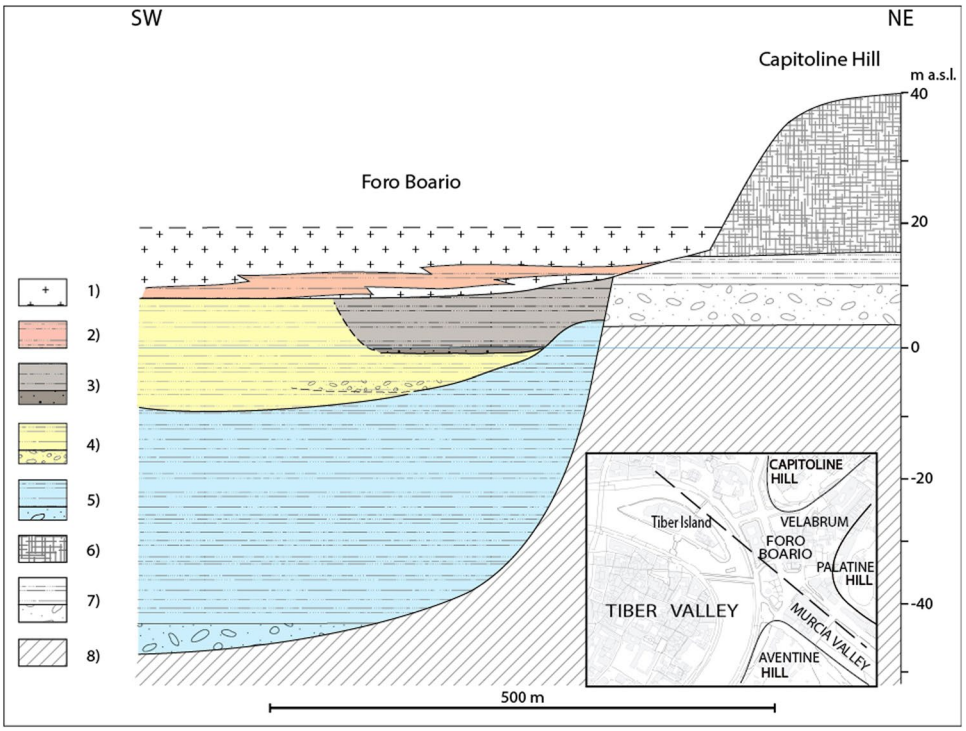

Fig. 1 Stratigraphic sketch showing the sedimentary filling of the Tiber River alluvial valley in the City of Rome. 1) Anthropic fill and modern alluvia; 2) Early Republican age alluvial deposits; 3) sixth century alluvial succession; 4) Bronze Age alluvial succession (5.500–2.800 years/BP); 5) pre-Bronze Age alluvial succession (18.000–5.500 years/BP); 6) Volcanic rocks; 7) Middle Pleistocene sedimentary deposits; 8) Plio-Pleistocene marine clay substrate

(Fig. 1). The origin of this unconformity, whether climatic, isostatic, or tectonic, has been discussed in Marra et al. (2013) ("mid-Holocene transgression") and its analysis is beyond the scope of the present work. The deposition of this later aggradational succession, characterized by lower sedimentation rates, started around 4500 years/BP and continued at least until 2800 years/BP, according to ^{14}C dating of interbedded organic materials (Marra et al. 2013, 2018).

A sudden increase in the sedimentation rate from around 2600 years/BP (i.e., sixth century BCE) is documented by the deposition in less than one century of a package of clayey sediments up to 6 m thick in the sector of the river valley inside the ancient city. These sediments overly a medium sized gravel layer ca. 10 cm thick, attesting to a temporary increase in transport capacity due to the establishment of a riverbed in this sector of the valley (Marra et al. 2018).

We have suggested that such sedimentary processes could be the result of a faulting process that caused the diversion of the river channel and the lowering of the fault's hanging wall. The increased accommodation space was then quickly filled by fine-grained alluvial sediments as a consequence of the loss in transport capacity by the shifting river. This change in the river regime could have also triggered the formation of the Tiber Island along the fault scarp. Combined ^{14}C dates and archaeological ages constrain this process between 2550 and 2450 years/BP (mid-sixth–fifth century BCE) (Marra et al. 2018).

Other authors (e.g., Luberti et al. 2018) have hypothesized that the reduction of the velocity of the Tiber River might have been induced by the counter-flow waters provided by the Murcia Valley tributary. However, the very small watercourse flowing in the Murcia Valley and the necessity for it to maintain a straight NW–SE course throughout its terminal tract, makes this hypothesis unlikely. On the other hand, the alignment of the two watercourses could have been possible if their beds were both controlled by the fault, making the hypotheses of the counter-flow waters not conflicting with the fault hypothesis.

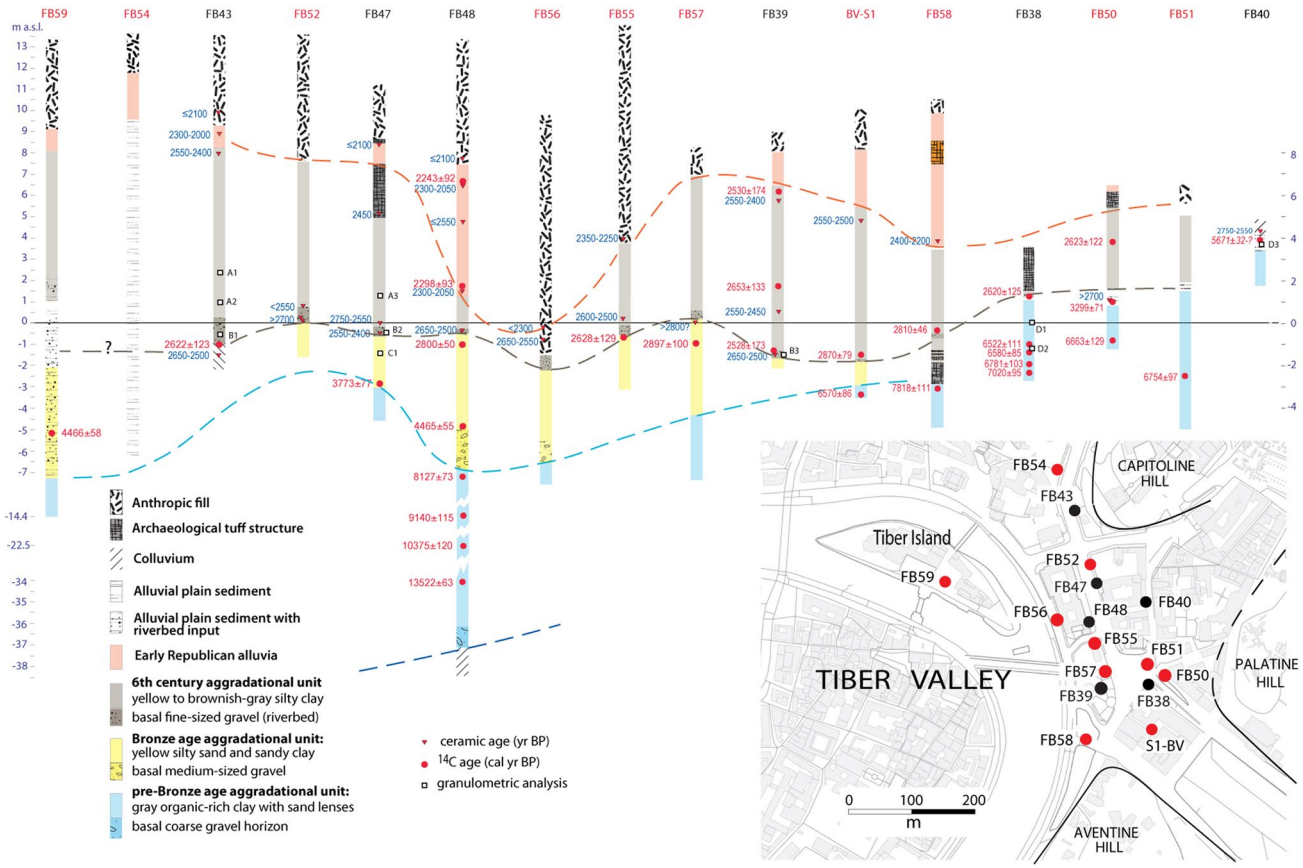

Fig. 2 Summary cross section showing the stratigraphy, the ^{14}C ages, and the archaeological dates achieved in the boreholes performed for the present study (red labels) and those published in Marra et al. (2018), employed in the reconstruction presented in this paper. See text for comments and detailed explanation

Materials and methods

To verify the actual occurrence of the hypothesized faulting process affecting the alluvial sediments of the Tiber River, the scale of its displacement, and its chronology, a new dedicated drilling campaign was planned in 2019 and aimed at providing new chronostratigraphic markers. In Fig. 2, we show the location of the ten new boreholes. The stratigraphic logs summarize the results of the sedimentologic and stratigraphic analysis of the ten new cores and the ones previously published in Marra et al. (2018).

Granulometric analysis

Granulometric analyses have been performed on 10 representative samples of the main stratigraphic units to provide a quantitative assessment of the paleo-environments and of the energy of the depositional system.

The analysis was carried out at the Free University of Amsterdam using the laserscan technique for the estimation of the grain size distribution of the fraction < 2 mm. This technique uses the differences in sedimentation velocity of the various size fractions, measuring through the laser the declining concentration of particles in suspension over time. To apply this technique, the fraction > 2 mm that settles too rapidly is preliminarily removed by sieving. We use the grain size distribution of the < 2 mm fraction to establish depositional environments characterized by different energy, while we provide visual evidence of the occurrence of the > 2 mm fraction (gravel) in one specific recurring stratigraphic layer. This is a characteristic coarse-grained layer which was identified in 4 cores during the previous drilling campaign, dated through combined ^{14}C and ceramic ages at ca. 2550 years/BP and interpreted as the sixth century BCE riverbed (Marra et al. 2018). We have recovered this layer in 6 new cores and we have provided three ^{14}C and three archaeological new age constraints to it.

Radiocarbon and archaeological dating

Every major stratigraphic component in each core was sampled for the retrieval of organic material suitable for radiocarbon dating. Sediments between the "Mid-Holocene transgression" and the Roman anthropic fills were the main target for sampling to obtain better chronological constraints for the faulting process and the morphological transformations in this part of the Tiber Valley. However, a few samples from the plant rich deposits characterizing the earlier estuarine environment were also collected to provide a lateral correlation between the two sets of cores. Wet sieving of the samples was carried out in the field with a 0.5 and a 1 mm mesh. Alluvial deposits very rich in clay were pretreated with sodium bicarbonate and then floated. The remains were sorted and identified in the bioarchaeology lab at the Kelsey Museum of Archaeology, University of Michigan using a 10–40X stereo zoom microscope. Priority for ^{14}C dating has been given to seeds, when not available to wood/charcoal or animal bones. The radiocarbon analysis was performed at the Chrono Lab at Queen University, Belfast.

All the ceramic fragments and other anthropic inclusions visible in the sediments were collected and recorded. Particular attention has been paid to the ceramic classes that define the transitional period between the end of the Bronze Age and the Iron Age (3000–2600 BP), such as *Impasto Bruno* and *Impasto Rosso.* In particular, *Impasto Rosso* is a good chronological marker with a limited time range (i.e., 2700–2550 BP).

While the anthropic fills were sampled and screened as well for organic remains, they usually provided abundant ceramic shards that offer a tighter chronological resolution than radiocarbon ages. In addition, ceramic dating was preferred for these deposits, since it is easier to identify reworked and residual ceramic fragments that are the majority of the material in a Roman period anthropic fill.

Paleomagnetic sampling, laboratory procedures, and analysis

Previous investigations highlighted the presence of a clay layer, 2–3 m thick, characterized by a strong disturbance of the Characteristic Remanent Magnetization (ChRM) inclination values measured on discrete samples (Marra et al. 2018). A clay layer recovered in a new borehole (FB50) was considered stratigraphically equivalent. In the present study, we have performed paleomagnetic and rock magnetic investigations to provide further stratigraphic markers for correlation and to understand the nature and the origin of this anomaly. The detailed methodological approach is described in Supplementary Material #1.

Micromorphological analysis

Soil micromorphology is the analysis of soil and sediment samples in thin section under the polarizing microscope. Samples are collected from a block of undisturbed and oriented soil, so that all the components of the soil maintain their original position. Micromorphological analysis has been performed on two clay samples yielding, respectively, anomalous and regular paleomagnetic inclination, with the aim of verifying the origin of the anomalous ChRM inclination values. In particular, we wanted to test the possibility that such low inclinations anomaly were due to the microsedimentary features of the analyzed sediment samples. The thin sections were produced according to standard methods

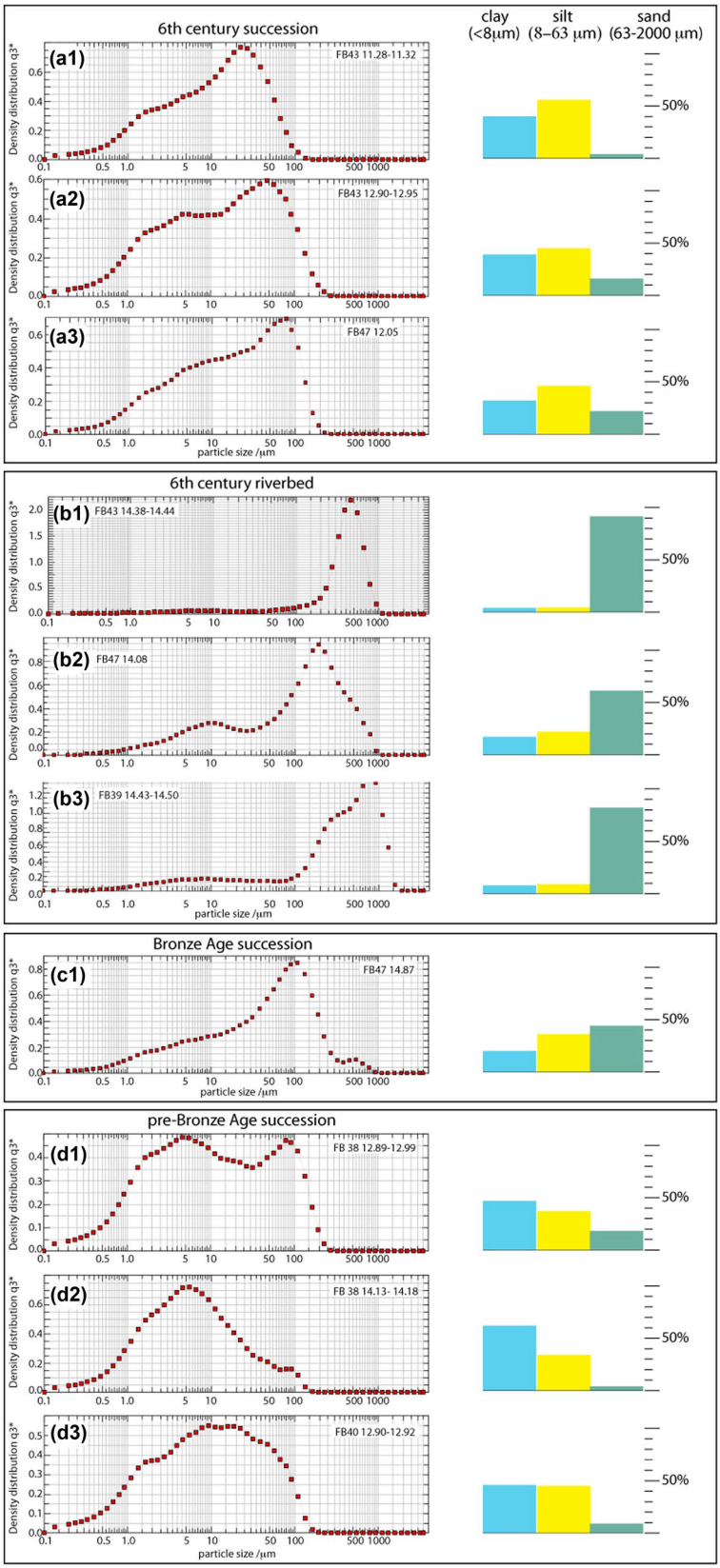

Fig. 3 Granulometric curves and main grain size classes' histogram distribution of 10 representative samples from the four stratigraphic horizons of the Tiber River alluvial succession defined in the present work. Full granulometric data are provided in Suppl. Mat. #1

(Meer 1986) and described according to the terminology of Stoops (2003).

Results

Granulometric analysis

Figure 3 shows the granulometric curve for the 10 analyzed samples and the percentage distribution of the three main granulometric classes (sand, silt, clay). Full analytical data are provided in Supplementary Material #2.

The idiosyncratic riverbed layer, besides being the only stratigraphic horizon characterized by the occurrence of a > 2 mm, gravel fraction (Fig. 4), yielded a largely prevalent sand matrix (65 to 90%), with little to very little (35–10%) finer fraction (sample B1–3, Fig. 3). This layer attests to a sudden increase in transport capacity by the river when compared with the underlying, Bronze-age sedimentary horizon (sample C1) which, instead, is distinguished by a prevalent (56%) < 2 mm fraction. An even more drastic grain size switch, indicating a sharp reduction in capacity of transport, occurs immediately above the riverbed layer. This sedimentary succession (samples A1–3) is defined by a largely prevalent fine fraction (40–46% clay, 45–55% silt), and a scanty (20 to 5%) sand fraction. The last group of samples belongs to the pre-Bronze age succession (samples D1–3) and is characterized by very fine sediments, with prevailing clay (45 to 60%) and abundant silt (35 to 45%) fractions, and a minor (20 to 5%) sand fraction.

The succession of sedimentary deposits represented by the sample groups D, C, B, A (Fig. 3) supports our interpretation of a mainly lacustrine environment by 6000 years/BP (pre-Bronze age succession), followed by the deposition of fluvial sediments in an alluvial plain environment (Bronze-age succession) (Marra et al. 2013, 2018). The sudden input of coarse fluvial sediment, represented by samples B1–3, is consistent with the establishment of a riverbed in this sector, while the overlying clayey-silt deposits evidence a sharp change of the depositional context, caused by sudden drop in capacity of transport as the river shifted away from this zone in the sixth century BCE.

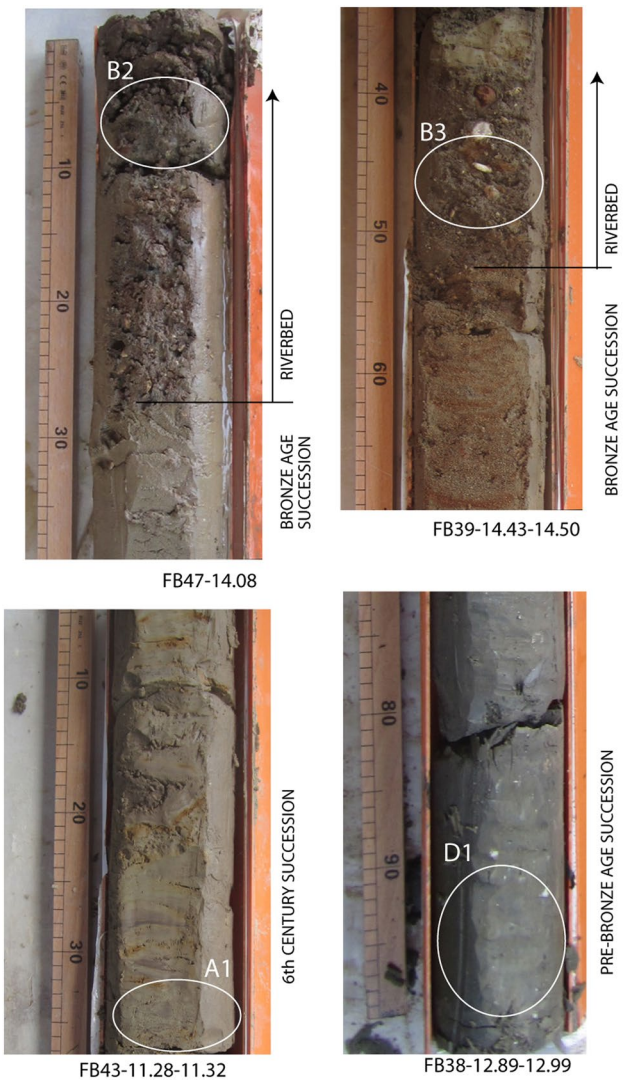

Fig. 4 Pictures of core portions, where samples, representative of the four main stratigraphic horizons defined in the present work, were collected for granulometric analysis

Chronological markers

Table 1 presents the new archaeological dates and radiocarbon ages acquired for the present work; it also summarizes the relevant chronological markers provided in Marra et al. (2018). All radiocarbon ages are calibrated according to Intcal13.14c. Dates are included in Fig. 2, where they are reported in year/BP range for the archaeological ones and as 2 sigma calibrated mean value ± the age span, for ^{14}C. BP is calculated from 1950.

Dates not in sequence and/or inverted have been discarded. In particular we discuss below four ^{14}C ages included in the illustrations (see Fig. 2 for a summary) that are considered problematic or not reliable.

FB40-12.74

The radiocarbon analysis was performed on concentrated pollen retrieved from a 6 cm thick section of sediment due to the lack of any other datable material. However, recent preliminary palynological analysis on those sediments revealed some eroded pollen in the assemblage, including Pliocene–Pleistocene flora. Likely, the presence of pollen from the eroded clay substrate (see Fig. 1 unit 8) produced

Table 1 Chronological markers

Core	Cut	Depth (m)	Elevation (masl)[1]	Chronological marker	Material	Calendar year BCE BP		Calibrated ^{14}C age BP (2σ)	^{14}C age BP (± SEM)	Lab code
FB 38	8	7.30	5.64	Archaeological	Mortar	After 150	≤ 2100			
	10	9.25	3.69	Archaeological	Republican sherd	Late 4th-early 1st c	2300–2050			
	12	*11.62–11.73*	*1.32–1.21*	*Archaeological*	*Post-archaic sherd*	*4th-1st c*	*2350–1950*			
	12	11.72–11.78	1.22–1.16	^{14}C	Waterlogged seeds	795–545	2745–2495	2620 ± 125	2530 ± 30	Beta 449,392
	15	14.03–14.43	− 1.09 to − 1.49	^{14}C	Sorted pollen	4683–4461	6633–6411	6522 ± 111	5716 ± 42	DSH 7887
	15	14.72–14.77	− 1.78 to − 1.83	^{14}C	Waterlogged wood- above ground	4715–4545	6665–6495	6580 ± 85	5790 ± 30	Beta 449,393
	16	15.20–15.24	− 2.26 to − 2.30	^{14}C	Waterlogged wood- above ground	4934–4727	6884–6677	6781 ± 103	5950 ± 40	GrA 66,073
	16	15.73–15.76	− 2.79 to − 2.82	^{14}C	Waterlogged wood-above ground	5215–5025	7165–6975	7020 ± 96	6170 ± 30	Beta 424,137
FB 39	5	4.55	8.23	Archaeological	Mortar	After 150	≤ 2100			
	7	6.70–6.80	6.08–5.98	^{14}C	Charcoal	755–405	2705–2355	2530 ± 175	2440 ± 30	Beta 431,184
	8	7.10	5.68	Archaeological	Archaic sherd	600–450	2550–2400			
	12	11.18–11.22	1.60–1.56	^{14}C	Bone, mammal	785–520	2735–2470	2603 ± 133	2500 ± 30	Beta 449,394
	13	12.36	0.42	Archaeological	Archaic sherd	600–450	2550–2400			
	15	14.25	− 1.47	^{14}C	Bone, tortoise	750–405	2700–2355	2528 ± 173	2430 ± 30	Beta 424,138
	15	14.34	− 1.56	Archaeological	Impasto Rosso	700–550	2650–2500			
FB 40	6	5.75	10.93	Archaeological	Mortar	After 150	≤ 2100			
	7	6.48	10.20	Archaeological	Post-Orientalizing sherd	After 600	≤ 2100			
	9	8.42–8.52	8.26–8.16	Archaeological	Etrusco-Corinthian pottery	700–500	2650–2450			
	10	*9.00–9.10*	*7.68–7.58*	*^{14}C*	*Charcoal*	*1050–910*	*3000–2860*	*2930 ± 70*	*2830 ± 30*	*Beta 422,662*
	12	11,40	5.28	Archaeological	Bucchero	700–500	2650–2450			
	13	12.40–12.50	4.28–4.18	Archaeological	Iron Age/ Orientalizing sherd	800–600	2750–2550			
	13	12.74	3.94	^{14}C	Sorted pollen	3703–3693	5653–5589	5621 ± 32	4879 ± 28	DSH 7836
FB 43	4	3.92	9.78	Archaeological	Mortar	After 150	≤ 2100			
	5	4.90	8.80	Archaeological	Republican sherd	250–100	2300–2050			
	6	5.57–5.75	8.13–7.95	Archaeological	Archaic sherd	600–450	2550–2400			
	6	5.65–5.85	8.05–7.85	Archaeological	Archaic sherd	600–500	2550–2450			
	15	14.80–14.85	− 1.10 to − 1.15	^{14}C	Plant material	795–550	2745–2500	2622 ± 123	2540 ± 30	Beta 424,139
	16	15.05	− 1.35	Archaeological	Impasto Rosso	700–550	2650–2500			
	16	15.80	− 2.1	Archaeological	Impasto Rosso	700–550	2650–2500			
FB 47	6	5.42	8.01	Archaeological	Mortar	After 150	≤ 2100			
	9	8.50	4.93	Archaeological	Late Archaic building phase	ca. 480	~ 2430			
	9	*8.80–8.90*	*4.63–4.53*	*^{14}C*	*Plant material*	*1625–1500*	*3575–3450*	*3513 ± 63*	*3280 ± 30*	*Beta 422,664*
	10	*9.60*	*3.83*	*^{14}C*	*Organic sediment*	*3355–3095*	*5305–5045*	*5175 ± 130*	*4510 ± 30*	*Beta 430,834*

Table 1 (continued)

Core	Cut	Depth (m)	Elevation (masl)[1]	Chronological marker	Material	Calendar year BCE BP		Calibrated ^{14}C age BP (2σ)	^{14}C age BP (± SEM)	Lab code
	12	*11.65–11.70*	*1.78–1.73*	*^{14}C*	*Plant material*	*805–765*	*2755–2715*	*2735 ± 20*	*2580 ± 30*	*Beta 422,665*
	14	*13.80–14*	*− 0.37 to − 0.57*	*Archaeological*	*Iron Age/ Orientalizing sherd*	*800–600*	*2750–2550*			
	15	14.10–14.13	− 0.67 to − 0.70	Archaeological	Archaic sherd	600–450	2550–2400			
	15	14.15–14.25	− 0.72 to − 0.82	Archaeological	Archaic sherd	600–450	2550–2400			
	17	16.55	− 3.12	^{14}C	Plant material	1900–1745	3850–3695	3773 ± 77	3500 ± 30	Beta 422,666
FB 48	6	5.85	7.64	Archaeological	Mortar	After 150	≤ 2100			
	7	6.80–7.0	6.69–6.49	^{14}C	Charred seeds	385—200	2335–2150	2243 ± 92	2230 ± 30	Beta 431,186
	8	7.10	6.39	Archaeological	Republican sherd	350—100	2300–2050			
	8	*7.05–7.30*	*6.44–6.19*	*Archaeological*	*Archaic/Republican sherd*	*After 600*	*≤ 2550*			
	8	*7.35*	*6.14*	*Archaeological*	*Iron Age/ Orientalizing sherd*	*800–600*	*2750–2550*			
	8	*7.65*	*5.84*	*Archaeological*	*Archaic/post-archaic*	*600–300*	*2550–2250*			
	9	*8.3*	*5.19*	*Archaeological*	*Archaic/post-archaic*	*600–300*	*2550–2250*			
	9	*8.84*	*4.65*	*Archaeological*	*Archaic/post-archaic*	*600–300*	*2550–2250*			
	12	11.05–11.15	2.40	Archaeological	Republican sherd	Late 4th-early 1st c	2300–2050			
	12	11.86	1.63	^{14}C	Waterlogged wood- above ground	390–205	2340–2155	2298 ± 93	2240 ± 30	Beta 449,395
	13	12.2	1.29	Archaeological	Republican sherd	Late 4th-early 1st c	2300–2050			
	15	14.08	− 0.59	Archaeological	Orientalizing sherd	700–550	2650–2500			
	15	14.70–14.71	− 1.21	^{14}C	Plant material	900–800	2850–2750	2800 ± 50	2690 ± 30	Beta 424,140
	19	18.6	− 5.11	^{14}C	Carbonized plant material	2570–2460	4520–4410	4465 ± 55	3980 ± 30	Beta 430,836
	20	20	− 6.51	^{14}C	Plant material	6215–6050	8165–8000	8082 ± 83	7250 ± 30	Beta 422,668
	21	21	− 7.51	^{14}C	Plant material	6250–6105	8200–8055	8127 ± 73	7350 ± 30	Beta 422,669
	29	28.4	− 14.91	^{14}C	Plant material	7305–7075	9255–9025	9140 ± 115	8180 ± 30	Beta 430,835
	37	36.7	− 23.21	^{14}C	Plant material	8545–8305	10,495–10,255	10,037 ± 120	9210 ± 30	Beta 422,670
	49	48.60	− 35.11	^{14}C	Carbonized plant material	11,635–11,510	13,585–13,460	13,522 ± 63	11,720 ± 40	Beta 425,692
FB 49	19	18.70	− 1.05	Archaeological	Mortar	After 150	≤ 2100			
	19	18.77	− 1.12	Archaeological	Orientalizing/Archaic sherd	700–500	2650–2450			
	19	18.95	− 1.30	Archaeological	Archaic sherd	600–450	2550–2400			
FB 50	11	10.18	6.66	Archaeological	Mortar	After 150	≤ 2100			
	13	12.95–13	3.84	^{14}C	Waterlogged grape seeds	795–550	2745–2500	2623 ± 122	2535 ± 25	UBA-42974
	16	15.85	0.99	Archaeological	2 impasto bruno sherds	Before 700	≥ 2700			
	16	15.84–15.89	0.95	^{14}C	Mammal bone	1420–1278	3370–3228	3299 ± 71	3087 ± 27	UBA-42982
	18	17.6	− 0.76	^{14}C	Waterlogged wood	4842–4584	6792–6534	6663 ± 129	5859 ± 50	UBA-42973
FB 51		6.08	6.53	Archaeological	Mortar	After 150	≤ 2100			

Table 1 (continued)

Core	Cut	Depth (m)	Elevation (masl)[1]	Chronological marker	Material	Calendar year BCE BP		Calibrated ^{14}C age BP (2σ)	^{14}C age BP (± SEM)	Lab code
		15.07–15.12	− 2.51	^{14}C	Waterlogged wood	4901–4707	6851–6657	6754 ± 97	5917 ± 40	UBA-42971
FB 52		5.85	7.62	Archaeological	Mortar	After 150	≤ 2100			
		12.87	0.6	Archaeological	Coarse ware sherd	After 600	≤ 2550			
		12.99	0.48	Archaeological	Impasto Bruno sherd	Before 700	≥ 2700			
		13.48	− 0.01	Archaeological	Impasto Bruno sherd	Before 700	≥ 2700			
FB 54	3	2.27	11.3	Archaeological	Mortar	After 150	≤ 2100			
	4	3.80–3.92	9.7	Archaeological	Republican sherds	4th-3rd c	2300–2150			
FB 55		9.58–9.59	4.3	Archaeological	Republican sherd	Mid 4th–mid 3rd	2300–2200			
		13.31	0.57	Archaeological	Impasto Rosso	650–550	2600–2500			
		14.54–14.60	− 0.72	^{14}C	Waterlogged plant material	807–549	2757–2499	2628 ± 129	2562 ± 35	UBA-42977
FB 56		18.1	− 0.34	Archaeological	Republican sherd	After 200	≤ 2150			
		18.49	− 0.73	Archaeological	Impasto Rosso	650–550	2600–2500			
FB 57		5.62–5.66	7.04	Archaeological	Republican sherd	3rd c	2250–2150			
		12.30–12.42	0.3	Archaeological	Iron Age sherd?	9th-8th c.?	2850–2700?			
		13.75	− 1.07	^{14}C	Waterlogged wood	1047–846	2997–2796	2897 ± 100	2803 ± 36	UBA-42972
FB 58		12.13–12.20	3.87	Archaeological	Republican sherd	4th-3rd c	2300–2150			
		12.17	3.87	Archaeological	Republican sherd	4th-3rd c	2300–2150			
		13.45–13.46	2.59	Archaeological	Post-Orientalizing sherd	After 600	≤ 2550			
		16.4	− 0.36	^{14}C	mammal bone	906–813	2856–2763	2810 ± 46	2713 ± 25	UBA-42979
		19.03	− 2.99	^{14}C	Waterlogged wood	5979–5757	7929–7707	7818 ± 111	6979 ± 36	UBA-42978
FB 59		19.61–19.66	− 5.1	^{14}C	Waterlogged seeds	2574–2457	4524–4407	4466 ± 58	3974 ± 27	UBA-42970
BV-S1		12.75	4.75	Archaeological	Archaic sherds	550–500	2500–2450			
		19.05	− 1.55	^{14}C	Charred seed	999–842	2949–2792	2870 ± 79	2775 ± 30	UBA-42981
		20.90	− 3.4	^{14}C	Waterlogged wood	4706–4535	6656–6485	6570 ± 86	5763 ± 33	UBA-42980
SO22	*2*	*1.66–1.83*	*5.79–5.62*	*^{14}C*	*Charred seed*	*1225–1045*	*3175–2995*	*3085 ± 90*	*2940 ± 30*	Beta 393,853
	3	*2.25–2.47*	*5.20–4.98*	*^{14}C*	*Charred seed*	*1205–1005*	*3155–2955*	*3055 ± 100*	*2900 ± 30*	Beta 393,850
SO24	4	4.11–4.20	3.28–3.19	^{14}C	Charred seed	1115–930	3065–2880	2972 ± 93	2860 ± 30	Beta 393,852
	4	4.25–4.36	3.14–3.03	^{14}C	Charred seed	1220–1020	3170–2970	3070 ± 100	2930 ± 30	Beta 393,851
SO32	5	5.69	7.17	Archaeological	Iron Age sherd	800–700	2750–2650			
SO36	5	4.77–4.87	7.04–6.94	^{14}C	Charcoal	1505–1415	3455–3365	3410 ± 45	3190 ± 30	Beta 393,854

an average ^{14}C age on the concentrated material much older than the sediment itself.

FB50-17.6 The large error associated with the ^{14}C age is due to the low graphite content of the sample, resulting in a calibrated date with a broader range.

FB58-16.4

The older than expected date for the riverbed layer in FB58 can be explained as reworked material. The bone sample comes from the clay/alluvial deposits above the coarser riverbed level.

S1-BV-19.05

The charred material used for this ^{14}C analysis was extracted from one small clay agglomerate included within the fine gravel layer. Its reworked nature is, therefore, very likely.

Paleomagnetic investigations

The downcore variation of the ChRM inclination values measured on discrete sediment samples from borehole FB50 is shown in Fig. 5a, along with thin sections of two samples displaying opposite (normal to reverse) inclination values (Fig. 5b). ChRM inclination data indicates generally a normal magnetic polarity except for a stratigraphic interval characterized by a high-frequency alternation of normal and reverse polarity likely due to sedimentary disturbance and not representative of the geomagnetic field behavior.

The down-core variation of the other rock magnetic parameters measured for FB50 core and the results of some specific rock magnetic analyses are shown in Fig. 6.

Hysteresis loops indicate the presence of intermediate–low coercivity minerals, with coercive force (B_C) of ca. 10 mT. Thermomagnetic analyses show a shallow decrease in magnetic susceptibility at about 580 °C during the heating (red curves), which indicates the ubiquitous presence of Fe spinels with a composition similar to magnetite.

Results of the paleomagnetic investigations performed in core FB50 are compared with those obtained for cores FB38 and FB40 in Marra et al. (2018) (Fig. 7). Evident in all these three boreholes is a recurring layer, ca. 50 cm thick, characterized by a high-frequency alternation of normal and reverse polarity (yellow shaded intervals) within the pre-Bronze age clays but at a different absolute elevation.

Micromorphological analyses

Sample FB50-c21

The thin section displays a foliated structure with mm-thick layers characterized by slightly different granulometry (Fig. 5b-1). In particular, all the layers are characterized by

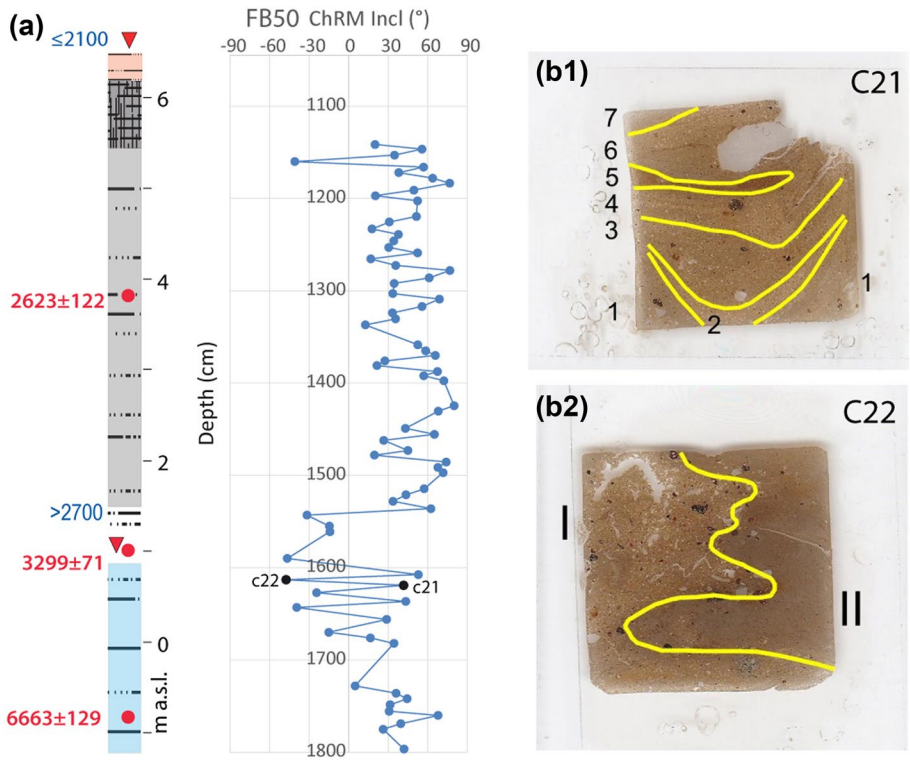

Fig. 5 **a** Lithostratigraphic column and downcore variation of the ChRM inclination values measured on discrete sediment samples in borehole FB50. **b** Thin sections for micromorphological study of the two samples, C21 and C22, investigated paleomagnetically (black dots in inset a; see also "Micromorphological analyses")

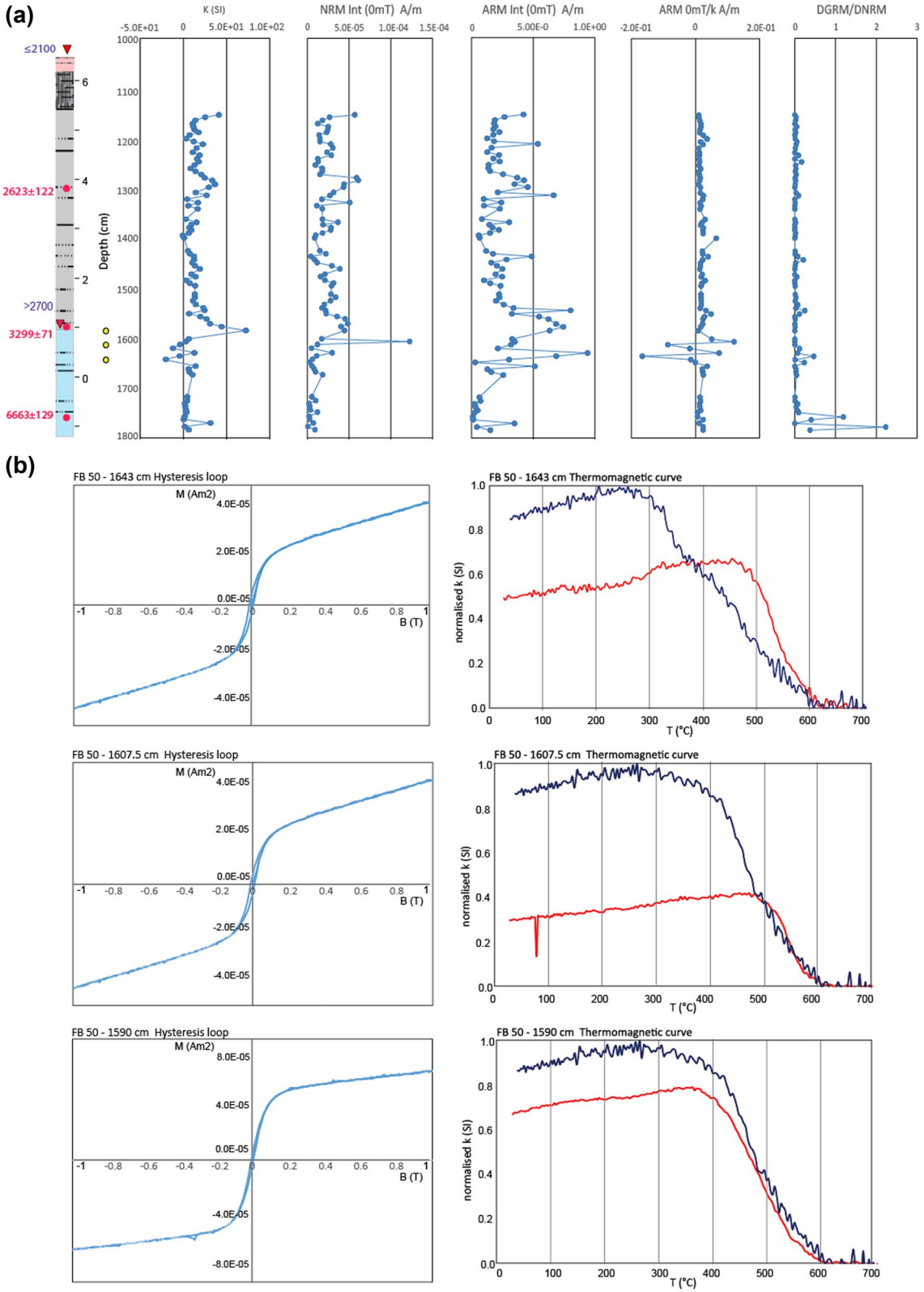

Fig. 6 **a** Stratigraphic variations of some rock magnetic parameters measured for the FB50 core. **b** Representative hysteresis loops and thermomagnetic curves for representative samples taken at different levels along the core (results for the sample at 1643, 1607.5 cm and 1590 cm depth, yellow dots)

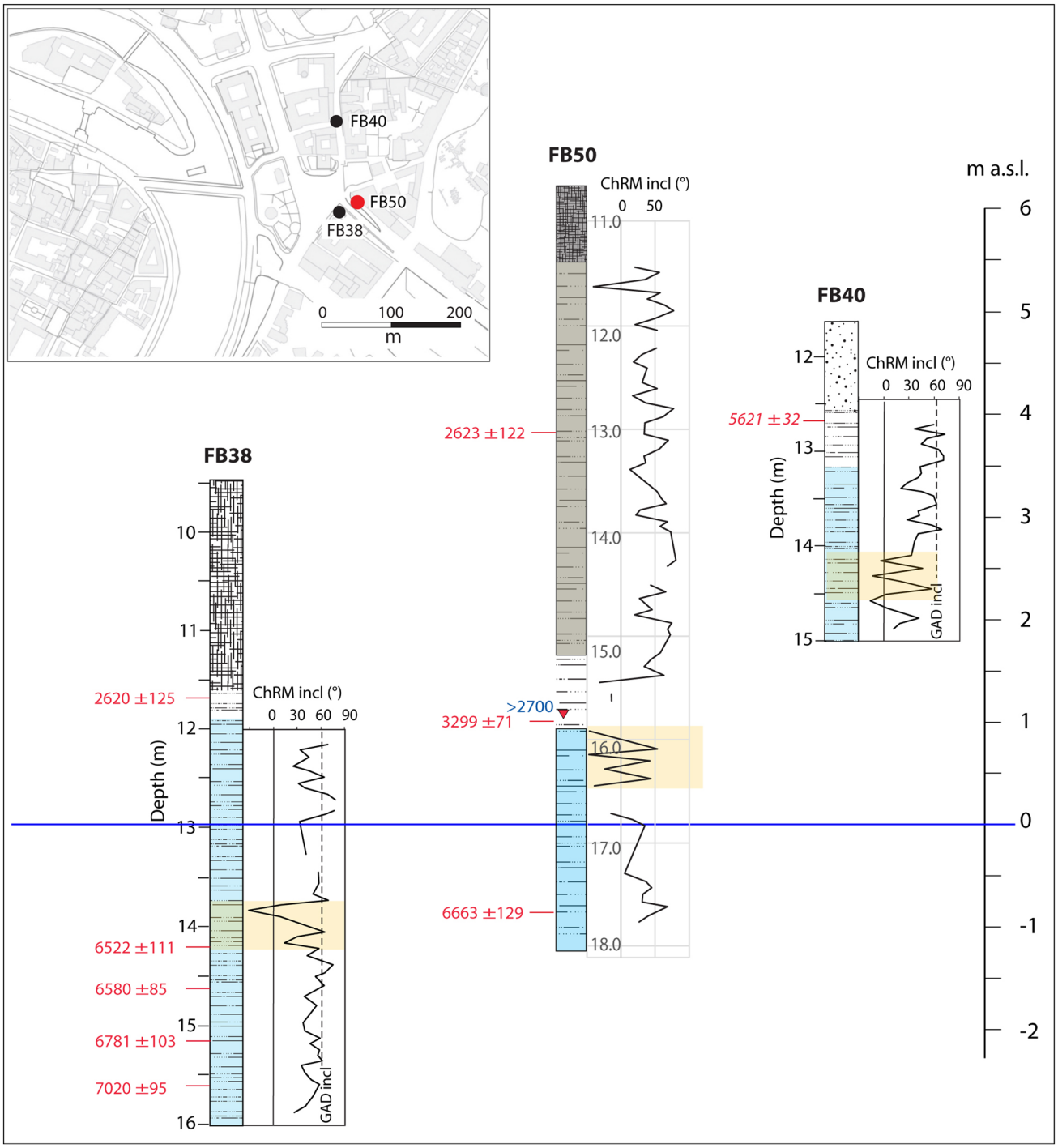

Fig. 7 Summary sketch showing the downcore variation of the ChRM inclination values measured on discrete sediment samples in FB50 (this work, see Fig. 5a) and in FB38, FB40 (Marra et al. 2018). Radiocarbon (red lines) and ceramic (red triangles) age constraints are also shown. Italicized age in FB40 is considered unreliable (see "Chronological markers")

a "frank" silt matrix with sand inclusions of different grain size. It makes exception layer 5, which has a finer, clayey-silty matrix.

The laminated appearance is an indicator of decantation in a low-energy environment. The sediments forming the sample are very compact and the voids almost absent (massive microstructure). The mineralogy of the various layers is quite homogeneous: the matrix is calcitic in nature and the mineral fragments are made up of quartz, mica, limestone

fragments, fragments of metamorphic rocks and volcanic scoriae.

Sample FB50-c 22

Unlike the previous sample, in this case no lamination is observed, but the thin section includes only two levels (Fig. 5b-2) which, apart from the rather homogeneous mineralogical composition, have different characteristics.

The layer I is constituted by silty sediments with a fine silty matrix of calcitic nature that includes fine sand fragments and scarce medium sand fragments. It is poorly compacted and displays bioturbation traces conferring a channeled microstructure to the layer (Kooistra and Pulleman 2010). In contrast, layer II has a massive microstructure and a finer, silty-clayey granulometry with very few, fine sand fragments. The mineral composition of both layers is the same as that of the layers in sample FB50-c21.

The structure observed in sample FB50-c22 should be interpreted as the effect of the disruption of the original sub-parallel layering, due to pore water overpressure. Such phenomenon is common in water-saturated sediments and may have different causes, including sedimentary load or seismic shaking (e.g., Shanmu 2016).

Chronostratigraphy

Based on the sedimentologic and chronostratigraphic data described above, we define the four main stratigraphic units (Table 2) that we use to describe the aggradational process affecting the continuous evolution of the Tiber River alluvial plain, building up the paleo-landscape of the river valley in the area of the Forum Boarium.

A ^{14}C age of 4466 ± 58 years/BP in borehole FB59 that was drilled on Tiber Island provides good lateral correlation with the Bronze age alluvial succession identified in the Forum Boarium. On the other hand, a continuous deposition of yellow clayey silt with frequent coarse sand and sparse fine gravel (≤ 1 cm in diameter) intercalations, in the interval -7 to 2 m a.s.l., makes it impossible to identify in the Tiber Island the boundary between the Bronze–Iron age and the sixth century BCE aggradational succession (Fig. 2).

Discussion

Evidence of fault displacement

Each of the defined chronostratigraphic units offer strong evidence of tectonic processes affecting the Forum Boarium. The following markers and reference layers are used to illustrate and constrain fault geometry and the scale of displacements:

1.pre-Bronze age blue clay setting. Age constraints: ^{14}C ages on wood and pollen. Stratigraphic marker: paleomagnetically disturbed horizon.
2. Bronze–Iron age yellow clay setting. Age constraints: ^{14}C ages on seeds, charcoal, plant material; archaeological ages on ceramic. Stratigraphic marker: Late Bronze age alluvial plain edge onlapping the pre alluvial pliopleistocene substrate of the Sant'Omobono terrace.
3. sixth century riverbed setting. Age constraints: ^{14}C ages on bone collagen, seeds, plant material. Archaeological dates on ceramic. Stratigraphic marker: coarse basal riverbed sedimentary layer.

pre-Bronze Age clay setting

These sediments, gray to bluish in color and deposited in response to rapid sea-level rise up to 6000 years/BP, represent an anoxic, fluvial–lacustrine environment as demonstrated by their granulometric composition and the micromorphological sample C21 (Figs. 3; 4; 5-b1). They include massive horizons alternating to finely laminated beds. Frequent peat layers and waterlogged vegetal remains occur throughout this thick sedimentary succession, with the exception the upper <6000 years/BP portion which is represented by highly plastic, light grey clay beds.

Paleomagnetic investigation of this clay section performed in boreholes FB38, FB40, FB50 reveal the occurrence of a ca. 50 cm thick layer characterized by a striking anomaly of the ChRM inclination (Fig. 7). In particular, a systematic inversion of the polarity affects several samples,

Table 2 Main chronostratigraphic units of the Tiber River alluvial deposits defined in the present study

Chronostratigraphic unit	Age (ka)
1) pre-Bronze age aggradational unit: basal coarse gravel horizon; gray organic-rich clay with sand lenses and frequent peat layers;	18–12.8; 12.8–5.5
Intervening sedimentary hiatus marked by an unconformity boundary (mid-Holocene transgression)	5.5–4.5
2) Bronze/Iron age aggradational unit: basal medium-sized gravel; yellow silty sand and sandy silt with dark brown, organic silt lamination;	ca. 4.5 4.5–2.8
3) sixth century aggradational unit: 3a) basal fine-sized gravel (riverbed); 3b) yellow to brownish-gray silty clay with fine lamination, lacking almost any anthropic inclusion	(2.8?)–2.55; 2.55–2.45

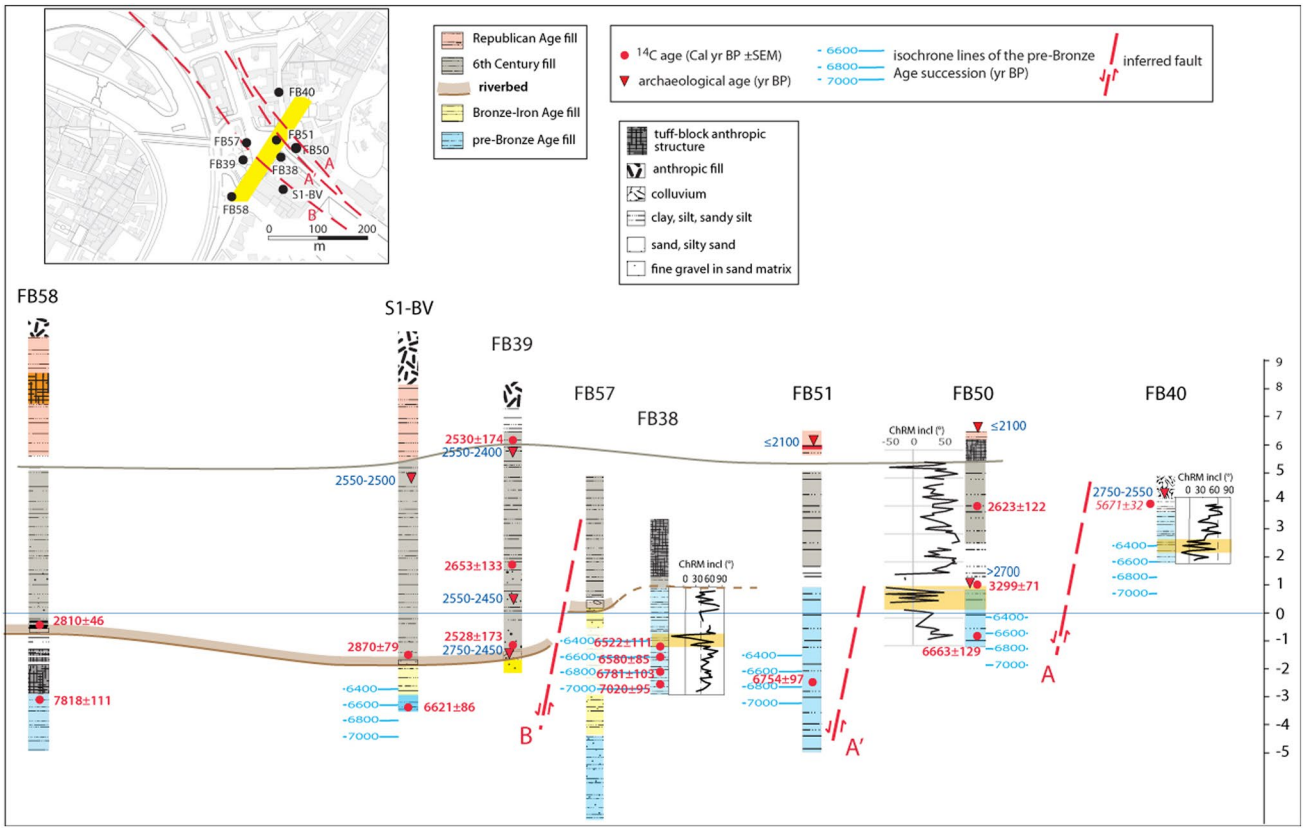

Fig. 8 Markedly different elevation of the paleomagnetically disturbed layer in boreholes FB40, FB50 and FB 38, combined with ^{14}C age constraints, are suggestive of a tectonic dislocation of the pre-Bronze age clay section. Three hypothetical faults (A, A', B) are proposed as the possible cause of displacement. See text for comments

each one comprised between two regular samples (Fig. 5a). Micromorphological analyses show that this anomalous paleomagnetic signal is generated by the disruption of the original, sub-horizontal foliation of the sedimentary structure when the sediment was still in a "plastic state" (Fig. 5b). We use this horizon as a *repere stratum* for correlation among the three boreholes.

New ^{14}C age determinations in boreholes FB50, FB51, FB58, S1-BV in addition to the four previously published for FB38 (Marra et al. 2018) allow us to reconstruct the chronostratigraphic setting of the pre-Bronze age clay succession in a transect perpendicular to the Tiber Valley (Fig. 8). By combining ^{14}C ages and paleomagnetic analysis, we have created a "chronologically constrained clay section" reference model in core FB38. This model is based on isochron lines, spanning 7000–6400 years/BP and determined by four in-sequence ^{14}C ages, that allow us to pinpoint the 6600 BP isochron at the base of the paleomagnetic anomaly.

The chronological scale is then reproduced at the base of the paleomagnetic anomaly in core FB50 and checked for consistency with the ^{14}C ages in this section. However, due to the large associated error, the calibrated age of sample FB50-17.6 (6663 ± 129 years/BP) covers almost the whole chronological interval of the reference section, providing neither a safe match nor a mismatch.

In contrast, the smaller age range associated with sample FB51-15.07 (6754 ± 97 years/BP) offers a tighter comparison with the chronological reference section, suggesting the lowering of the clay section recovered in FB51 with respect to that occurring in FB38. Similarly, the 6570 ± 86 years/BP age in S1-BV suggests lowering of the clay section also in this borehole, both with respect to FB38 and, more significantly, to the nearby core FB58, where at approximately the same elevation there is a 7818 ± 111 years/BP age (Fig. 8).

To be noted is the lack of reliable ^{14}C age constraints in FB40 that does not permit any geochronologic check on the hypothesized age for the paleomagnetic anomaly occurring in this core.

Bronze–Iron age yellow clay setting

Several shallow percussion cores drilled in the Sant'Omobono archaeological area (Brock and Terrenato 2016; Brock et al. 2021) depict a Late Bronze age

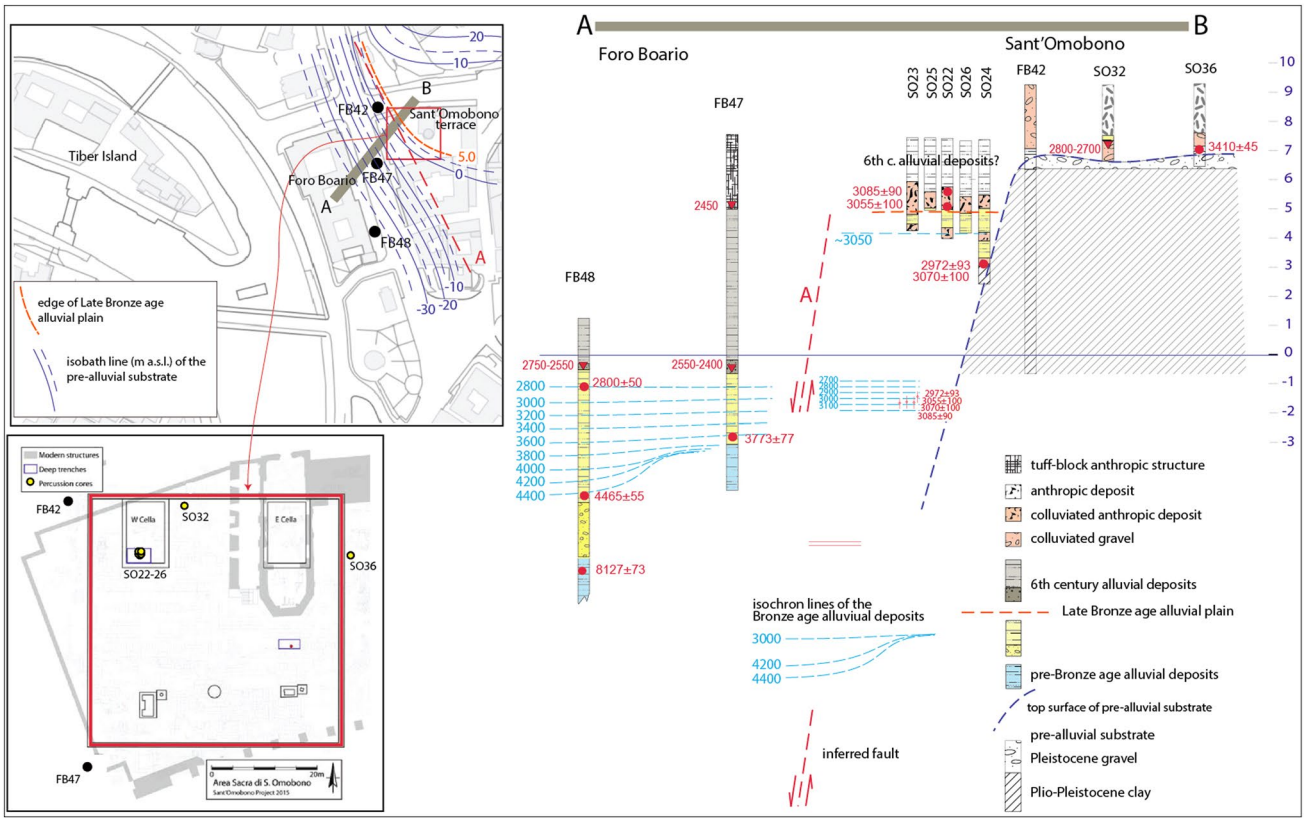

Fig. 9 Cross section A–B shows the occurrence of an alluvial plain edge at ca. 5 m a.s.l. in the Sant'Omobono area. Age constraints on this ca. 3-m thick alluvial succession highlight significant offset with respect to the coeval alluvial plain deposits recovered in the nearby Forum Boarium area, suggesting a possible tectonic dislocation caused by a fault (A)

paleolandscape characterized by a terraced morphology (Fig. 9). A dry, elevated northeastern sector, constituted by Middle Pleistocene sedimentary deposits, faced an alluvial plain located ca. 2 m below and periodically inundated. On top of the pre-alluvial horizon in this sector are material colluviated from the adjacent hill and dated by ^{14}C to 3410 ± 45 years/BP. In addition, at the western edge of the terrace an alluvial succession has been recovered between 5 and 3 m a.s.l., intercalated with heterogeneous deposits containing anthropic material, including ceramic sherds and seeds dated by ^{14}C to the eleventh century BCE (2972 ± 93—3070 ± 100 years/BP). Either dumped or colluviated, these deposits within the alluvial sequence both attest to a human presence in the general vicinity from the Late Bronze Age and provide *terminus post quem* ages suggesting a long stasis of aggradation process in the alluvial plain during the Late Bronze Age through the Early Iron Age (3000–2800 years/BP). Finally, a 2 m thick clayey succession, characterized by alluvial plain deposits occurs between 5.5 and 7.5 m a.s.l.. Elevation and lack of any anthropic material in these alluvial deposits suggest correlation with the sixth century overflooding of the Tiber Valley.

When the occurrence of an alluvial plain edge at + 3–5 m a.s.l. during the 3000–2800 year BP interval in the Sant'Omobono area is compared with the much lower elevation of the coeval alluvial plain deposits recovered at borehole FB47 and FB48 in the nearby Forum Boarium area, a possible tectonic dislocation caused by a fault line between these sectors (A in Fig. 9) is conceivable.

Sixth century riverbed

The retrieval in ten boreholes of a decimeter thick coarse basal layer indicates that the river was previously flowing east of its present position. The course of this riverbed layer and its top elevations are provided in the map, Fig. 10a; the cross section in Fig. 10b shows the lateral correlation among the cores in which the riverbed layer occurs.

The ceramic material in the newly performed FB52 and FB55 boreholes confirm a chronological range for this riverbed within the sixth century BCE (ca. 2550 years/BP), while ceramic ages in S1-BV provide new evidence to the rapid filling of the river channel up to 5 m a.s.l. by the late sixth

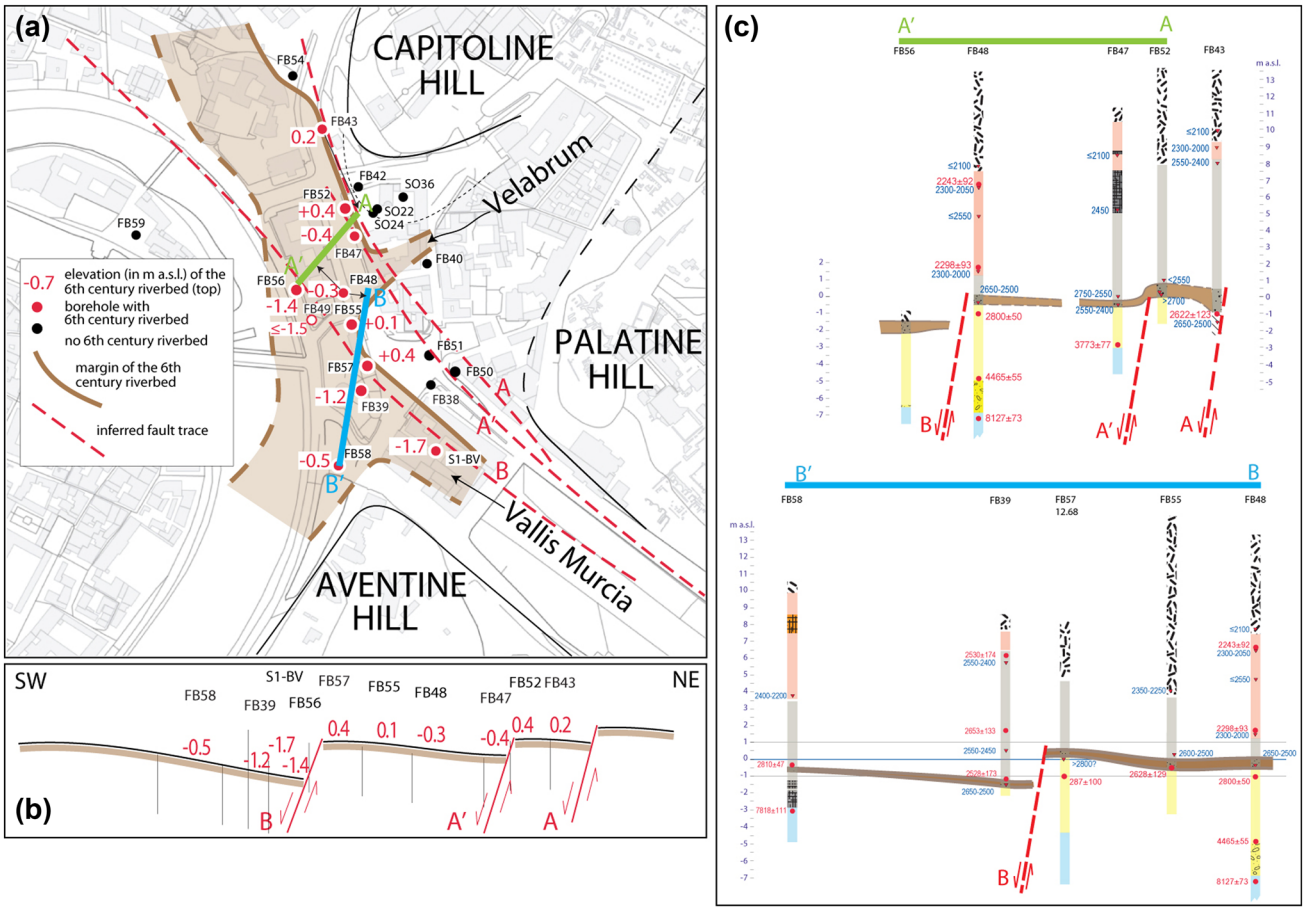

Fig. 10 **a** Map reconstruction of the riverbed layer's top in the investigated area; **b** sketch cross section (vertical not to scale) showing geometry compatible with tilting of faulted blocks, according to the position of the hypothesized fault lines (see text for explanation); **c** cross sections showing the offsets affecting the riverbed layer and the consistency with the hypothesized fault lines

century, as hypothesized in Marra et al. (2018). However, two new ^{14}C ages, in FB58 and S1-BV (2810 ± 46 years/BP and 2870 ± 79 years/BP), seem to push back the emplacement of the new riverbed in the southern sector of the investigated area to the beginning of the eighth century. Two explanations for the older than expected ^{14}C ages in FB58 and S1-BV are possible. First, it must be remarked that the dated material should be considered a *terminus post quem* for the age of the sediment in which it is embedded. Therefore, also given the straightforward lateral stratigraphic correlation of this thin layer among all the boreholes (Fig. 10), the two old ages may be attributed to reworked material, as already discussed in "Chronological markers". A second hypothesis is that the eastward shift of the riverbed could have occurred already around 2800 years/BP, possibly as a result of the early faulting of the Late Bronze age alluvial plain.

Figure 10 shows a sharp offset of the riverbed elevation between the northern and the southern sectors of the investigated area, where this layer occurs around the present sea level and −0.6 to −1.7 m, respectively. This sedimentary horizon is constituted by a 10–50 cm thick basal layer, characterized by a medium-to-coarse sand matrix with sparse fine gravel (≤ 2 cm in diameter) (see Figs. 3, 4). The only exception is in borehole FB43, where a finer gravel fraction (≤ 4 mm in diameter) is present in the upper, 10 cm-thick portion, above a ca. 1 m thick sand layer. This latter, in turn overlies colluvial clay and gravel. We attribute these peculiar features to the position of borehole FB43 at the hanging wall of fault A bordering the Tiber Valley to the east (Fig. 10).

Similarly, we attribute the abrupt offset of the riverbed layer south of core FB57 to the displacement caused by a second fault B (Fig. 10).

The new boreholes performed for the present study allow at constraining more closely the position of this fault in the map of Fig. 10a, consistent with its previously inferred NW–SE alignment with the Murcia Valley and the Tiber Island (Marra et al. 2018). Moreover, the location of the three fault traces A, A', and B is also in agreement with their inferred position in relation to the presumed dislocation of

the pre-Bronze age clay succession, as shown in the cross section of Fig. 8.

When the overall spatial variation of the riverbed top elevation is considered, a consistent deformation pattern with respect to the hypothesized fault traces is observed. This is based on the common notion of uplift at the footwall and tilting of the hanging wall of an extensional fault, as predicted by tectonic models and illustrated in Fig. 10b, where an NE–SW transect, perpendicular to the three fault plains, is presented. The three faulted blocks are tilted NE, according to the geometry of the SW-dipping, high angle normal faults A, A', B. Boreholes are projected on the faulted blocks roughly perpendicular to the profile, to maintain their position with respect to the fault planes. Indeed, the attitude of the riverbed layer matches the geometry of the faulted blocks, displaying progressive inclination towards the footwall of the three faults.

Paleogeographic evolution

By integrating all the evidence described in the previous sections, we attempt to depict an evolutionary process accounting for the transformation of an original Late Bronze–Early Iron Age landscape into the present chronostratigraphic setting in this portion of the Tiber Valley. To do so, we palinspastically restore an ideal transect across Sant'Omobono, the Forum Boarium, and the Tiber Island, constrained by the chronostratigraphic data acquired in 9 selected boreholes (Fig. 11). Several of these boreholes have been translated upwards with respect to their present-day elevation, with a variable elevation gain aimed at establishing a geo-morpho-chrono-stratigraphically consistent picture (Fig. 11-i). These translations are supposed to restore the subsequent fault displacements, responsible for creating the complex present setting shown in Fig. 11-v.

As shown in Fig. 9, present elevation of the Bronze–Iron age sedimentary succession spanning 4400–2800 years/BP recovered in FB48 (−5/−1 m a.s.l., Fig. 11-v) conflicts with occurrence of alluvial plain sediments dating 3000 years at + 3–5 m a.s.l. in Sant'Omobono.

By combining the reconstruction of an alluvial plain of ~ 2800 years/BP characterized by limited, geomorphologically plausible, varying elevation, with a sixth century riverbed layer that originally was necessarily at homogeneous elevation (Fig. 11-ii), we have assumed a progressively increasing dislocation of the boreholes, from 2 to 5.2 m in elevation gain, towards the center of the valley (Fig. 11-i). By restoring these offsets, we obtain a paleolandscape characterized by a gently dipping alluvial plain, onlapping the Sant'Omobono terrace on its western edge. This alluvial plain was initially created by continuous, steady sediment aggradation after the "Mid-Holocene transgression" until ~ 2800 years/BP, and by the following accretion of a sedimentary wedge (dashed lines) in the flooding area at the margin of the valley (Fig. 11-i).

Starting from this undeformed paleo-landscape, we suggest that a first fault displacement (A) might have been responsible for the ground deformation causing either the sudden or progressive shifting of the riverbed, previously located in the middle of the Tiber Valley, between the late 8th and the sixth century (Fig. 11-ii). Continued fault activity during the sixth century, propagating towards the center of the valley with a second fault segment (A'), would have generated the early offset of the riverbed between FB52 and FB 47, and the accelerated sediment accumulation to fill the newly created accommodation space (Fig. 11iii). Finally, the activation of a third fault segment (B) at the end of the sixth century, would have triggered the observed ~ 1 m dislocation of the riverbed layer (Fig. 10a), caused the westward backshift of the river course and contributing to the creation of the Tiber Island (Fig. 11iv). It is possible that anthropic interventions would have been necessary to prevent subsequent erosion of the island (Fig. 11v).

Conclusions and final remarks

The data and their interpretation presented in this study provide additional support for a fault system affecting the Tiber Valley in the Forum Boarium area. The different fault segments highlighted by the morpho-stratigraphic reconstructions should be considered part of a major NW–SE fault zone, originated by the extensional regime acting in Pleistocene times in this region (Montone and Mariucci 2016). Such segments are independently re-activated under the present-day weaker tectonic regime (Frepoli et al. 2010).

The present offset of the stratigraphic marker characterized by the ChRM inclination anomaly and by an originally sub-horizontal attitude, is consistent with the position of the inferred fault lines A and A'. The elevation at 3–5 m a.s.l. of the 3000 years/BP isochrone within the archaeological area of Sant'Omobono, when compared to the elevation of coeval alluvial plain deposits at −1 m in the nearby Forum Boarium, also suggest the occurrence of a tectonic displacement affecting this area after ca. 3000 years/BP. Moreover, indications of a 1 m displacement affecting the sixth century riverbed layer allows us to trace more precisely fault line B. This is a key-point to constrain in time (within the sixth century) and in space (the NW–SE trending fault line adjacent to the Tiber Island) the origin of the Tiber Island with the fault B activity, as previously hypothesized in Marra et al. (2018).

One important issue that needs to be investigated further is whether moderate to big earthquakes were associated with this fault activity. In this regard, the soft-sediment deformation structures affecting the pre-Bronze age clay succession

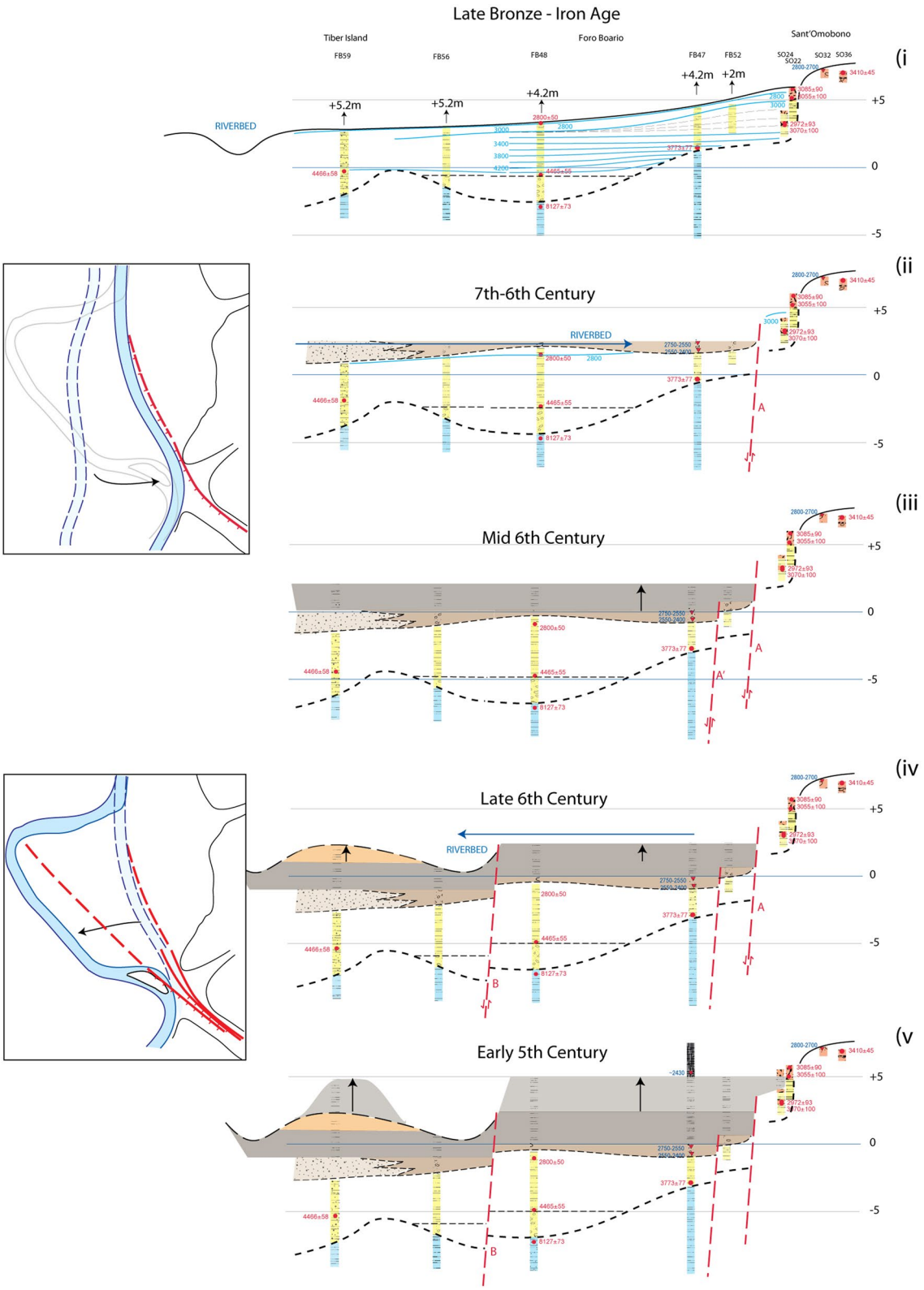

Fig. 11 NE–SW cross section showing the progressive evolution of the paleolandscape, according to borehole's data and to the interpretations discussed in this paper (see text for step-by-step description)

may be regarded as "seismites" (i.e., originated by seismic shaking; Shanmu, 2016). The occurrence of deformed layers sandwiched between undeformed layers (see Fig. 6) is indeed a major criterion for the identification of seismites (Seilacher 1969; Rodríguez-Pascua et al. 2000; Rodríguez-Lopezet al. 2007).

The seismic features of the several faults for which activity in the historical period has been hypothesized in the area of Rome is discussed in Marra et al. (2020) and is beyond the aims of the present work. Here we consider some specific aspects of the deformation picture outlined by this study. The inferred offset of up to 5 m for the paleolandscape reconstruction in Fig. 11 is a cumulative effect of a deformation that persisted for at least four centuries, spanning ~ 3000 to 2600 years/BP. However, the ca. 1 m offset affecting the sixth century riverbed layer may be considered as a relatively sudden event as indicated by the chronological markers. Such large displacements are generally associated with big earthquakes (e.g., $M \geq 6.5$, Wells and Coppersmith 1994), depending on the regional seismotectonic regime and on fault parameters. Based on the historical and instrumental records for the City of Rome, the maximum expected earthquake magnitude is $M_L = 5.6$ (Molin and Guidobobni 1989; Tertulliani and Riguzzi, 1995). The seven largest events reported in the Catalogue of Strong Earthquakes in Italy from 461 BCE to 1980 CE (Boschi et al. 1995) have an estimated local magnitude $> 5 \leq 5.5$. Therefore, unless we postulate a recurrence times > 2000 years, an aseismic, creeping behavior should be assumed for fault B. Creeping behavior, which is a common feature of large fault zones worldwide, is generally associated with cumulative aseismic deformation interpunctuated by seismic release during the long-term evolution of the fault surface (e.g., Kaduri et al. 2017). In particular, for faults in the area of Rome, creeping behavior may be regarded as consistent with the vertical tectonics acting in this region during the last 300 ka (Marra et al. 2019), that resulted in ca. 50 m uplift of the Tyrrhenian Sea margin in Central Italy (Marra et al. 2016b, 2017, 2019). Under such conditions, aseismic re-activation of small segments of pre-existing fault lines cannot be excluded. In this scenario, the observed 1 m slip might have been caused by an aseismic "slow earthquake" (e.g., Beroza and Ide 2011) that occurred within a time frame of several decades. Indeed, we cannot exclude that the observed offset was generated by a very slow deformation that occurred from the sixth century BCE through present time. In conclusion, the 5–6 m total offset inferred for the Forum Boarium should be regarded as a cumulated displacement that resulted from a progressive deformation along the different fault lines during three millennia, and that occurred with an average tectonic rate of 2 mm/year. This deformation process was likely interpunctuated with moderate earthquakes, as suggested by the seismites, but no large event necessarily occurred. A combination of climatic and anthropic causes might have triggered the subsequent overflooding of the Tiber Valley during the sixth century, an accelerated hydrologic regime that led to the emergence of the Tiber Island.

Supplementary Information The online version contains supplementary material available at https://doi.org/10.1007/s00531-021-02118-5.

Acknowledgements We are grateful to Soprintendenza Speciale di Roma and Sovrintendenza Capitolina ai Beni Culturali for authorizing the investigations, and to Elisabetta Bianchi, Elisabetta Carnabuci, Monica Ceci, Stefania Pergola, Renato Sebastiani for archaeological supervision and logistic support to the drilling campaign. P. Reimer and the Chrono Lab at Queen University, Belfast offered their precious help with radiocarbon dating. We thank Gian Marco Luberti and Andrea Tertulliani for their careful reviews and insightful suggestions. We also thank Maria Rita Caponi and Massimo Lenoci of CNG S.r.l. for carrying out a high-quality coring campaign.

Funding Open access funding provided by Istituto Nazionale di Geofisica e Vulcanologia within the CRUI-CARE Agreement. Research funding was provided by Loeb Classical Library Foundation, Gerda Henkel Foundation, American Philosophical Society, Etruscan Foundation, Fondazione Lemmermann, University of Michigan, University of St Andrews, and the Leverhulme Trust.

Availability of data and materials Data archiving is underway and will be openly available in PANGAEA (https://www.pangaea.de/). For review purposes, we uploaded our data as Supporting Information.

Code availability Not applicable.

Declarations

Conflict of interest The authors declare no conflict of interest/competing interests.

References

Beroza GC, Ide S (2011) Slow earthquakes and nonvolcanic tremor. Annu Rev Earth Planet Sci 39:271–296. https://doi.org/10.1146/annurev-earth-040809-152531

Boschi E, Ferrari G, Gasperini P, Guidoboni E, Smriglio G, Valensise G (1995) Catalogo dei forti terremoti in Italia dal 461 a.C. al 1980. Istituto Nazionale di Geofisica e Vulcanologia - Storia Geofisica e Ambiente, Bologna, Italia

Brock AL, Terrenato N (2016) Rome in the Bronze Age: late second-millennium BC radiocarbon dates from the Forum Boarium. Antiquity 90:654–664

Brock AL, Motta L, Terrenato N (2021) On the banks of the Tiber: opportunity and transformation in early Rome. J Roman Stud. https://doi.org/10.1017/S0075435821000344

Corazza A, Lanzini M, Rosa C, Salucci R (1999) Caratteri stratigrafici, idrogeologici e geotecnici delle alluvioni tiberine nel settore del centro storico di Roma. Il Quat 12:215–235

Del Monte M, D'Orefice M, Luberti GM, Marini R, Pica A, Vergari F (2016) Geomorphological classification of urban landscapes: the case study of Rome (Italy). J Maps 12:178–189

Frepoli A, Marra F, Maggi C, Marchetti A, Nardi A, Pagliuca NM, Pirro M (2010) Seismicity, seismogenic structures and crustal stress field in the greater area of Rome (Central Italy). J Geophys Res Solid Earth. https://doi.org/10.1029/2009JB006322

Kaduri M, Gratier J-P, Renard F, Çakir Z, Lasserre C (2017) The implications of fault zone transformation on aseismic creep: example of the North Anatolian Fault, Turkey. J Geophys Res Solid Earth. https://doi.org/10.1002/2016JB013803

Kooistra MJ, Pulleman MM (2010) Features related to faunal activity. In: Stoops G, Marcelino V, Mees F (eds) Interpretation of micromorphological features of soils and regoliths. Elsevier, Amsterdam, pp 397–418

Luberti GM, Vergari F, Marini R, Pica A, Del Monte M (2018) Anthropogenic modifications to the drainage network of Rome (Italy): the case study of the Aqua Mariana. Alpine Mediterr Q 31:119–132

Marra F, Florindo F (2014) The subsurface geology of Rome, Italy. Relationships among sedimentary processes, sea-level changes and astronomical forcing. Earth Sci Rev. https://doi.org/10.1016/j.earscirev.2014.05.001

Marra F, Bozzano F, Cinti FR (2013) Chronostratigraphic and lithologic features of the Tiber River sediments (Rome, Italy): implications on the Post-glacial sea-level rise and Holocene climate. Glob Planet Change. https://doi.org/10.1016/j.gloplacha.2013.05.002

Marra F, Rohling EJ, Florindo F, Jicha B, Nomade S, Pereira A, Renne PR (2016a) Independent 40Ar/39Ar and 14C age constraints on the last five glacial terminations from the aggradational successions of the Tiber River, Rome (Italy). Earth Planet Sci Lett. https://doi.org/10.1016/j.epsl.2016.05.037

Marra F, Florindo F, Anzidei M, Sepe V (2016b) Paleo-surfaces of glacio-eustatically forced aggradational successions in the coastal area of Rome: assessing interplay between tectonics and sea-level during the last ten interglacials. Quat Sci Rev. https://doi.org/10.1016/j.quascirev.2016.07.003

Marra F, Florindo F, Petronio C (2017) Quaternary fluvial terraces of the Tiber Valley: geochronologic and geometric constraints on the back-arc magmatism-related uplift in central Italy. J Sci Rep. https://doi.org/10.1038/s41598-017-02437-1

Marra F, Motta L, Brock AL, Macrì P, Florindo F, Sadori L, Terrenato N (2018) Rome in its setting. Post-glacial aggradation history of the Tiber River alluvial deposits and tectonic origin of the Tiber Island. Plos One. https://doi.org/10.1371/journal.pone.0194838

Marra F, Gaeta M, Jicha BR et al (2019) MIS 9 to MIS 5 terraces along the Tyrrhenian Sea coast of Latium (central Italy): assessing interplay between sea-level oscillations and tectonic activity. Geomorphology. https://doi.org/10.1016/j.geomorph.2019.106843

Marra F, Milana G, Pecchioli L et al (2020) Historical faulting as the possible cause of earthquake damages in the ancient Roman port city of Ostia. J Seismol 24:833–851. https://doi.org/10.1007/s10950-019-09844-z

Meer J (1986) Thin section preparation of soils and sediments. Murphy Publisher AB Academic Publishers, Berkhamsted

Molin D, Guidoboni E (1989) Effetto fonti, effetto monumenti a Roma: i terremoti dell'antichità a oggi. In: Guidoboni E (ed) I terremoti prima del Mille in Italia e nell'area mediterranea. Storia Geofis Ambiente, Bologna, pp 194–223

Montone P, Mariucci MT (2016) The new release of the Italian contemporary stress map. Geophys J Int. https://doi.org/10.1093/gji/ggw100

Rodríguez-Lopez JP, Merléndez N, Soria AR, Liesa CL, Van Loon AJ (2007) Lateral variability of ancient seismites related to differences in sedimentary facies (the syn-rift Escucha Formation, Mid-Cretaceous, Spain). Sed Geol 201:461–484

Rodríguez-Pascua MA, Calvo JP, De Vicente G, Gómez-Gras D (2000) Seismites in lacustrine sediments of the Prebetic Zone, SE Spain, and their use as indicators of earthquake magnitudes during the Late Miocene. Sed Geol 135:117–135

Seilacher A (1969) Fault-graded beds interpreted as seismites. Sedimentology 13:155–159

Shanmu G (2016) The seismite problem. J Palaeogeogr. https://doi.org/10.1016/j.jop.2016.06.002

Stanford JD, Hemingway R, Rohling EJ, Challenor PG, Medina-Elizalde M, Lester AJ (2011) Sea-level probability for the last deglaciation: a statistical analysis of far-field records. Glob Planet Change. https://doi.org/10.1016/j.gloplacha.2010.11.002

Stoops G (2003) Guidelines for analysis and description of soil and regolith thin sections, 2nd edn. John Wiley and Sons, New York

Tertulliani A, Riguzzi F (1995) Earthquakes in Rome during the past one hundred years. Ann Geofis. https://doi.org/10.4401/ag-4070

Wells DL, Coppersmith KJ (1994) New empirical relationships among magnitude, rupture length, rupture width, rupture area, and surface displacement. Bull Seismol Soc Am 84:974–1002